J|A|C|S ARTICLES

Published on Web 12/29/2009

Influence of Size on the Rate of Mesoporous Electrodes for Lithium Batteries

Yu Ren, A. Robert Armstrong, Feng Jiao, and Peter G. Bruce*

EaStChem and School of Chemistry, University of St Andrews, St Andrews, Fife KY16 9ST, U.K.

Received July 3, 2009; E-mail: p.g.bruce@st-andrews.ac.uk

Abstract: High power rechargeable lithium batteries are a key target for transport and load leveling, in order to mitigate CO_2 emissions. It has already been demonstrated that mesoporous lithium intercalation compounds (composed of particles containing nanometer diameter pores separated by walls of similar size) can deliver high rate (power) and high stability on cycling. Here we investigate how the critical dimensions of pore size and wall thickness control the rate of intercalation (electrode reaction). By using mesoporous β-MnO_2, the influence of these mesodimensions on lithium intercalation via single and two-phase intercalation processes has been studied in the same material enabling direct comparison. Pore size and wall thickness both influence the rate of single and two-phase intercalation mechanisms, but the latter is more sensitive than the former.

Introduction

The current appetite for high power rechargeable lithium batteries has led to considerable interest in nanostructured electrodes as a means of achieving the high electrode reaction rates required to deliver high power.[1−23] The electrode reaction in a rechargeable lithium battery relies on the simultaneous intercalation of Li^+ and e^- into the active intercalation host of a composite electrode. Many factors can influence the rate of intercalation and hence the power of the battery, including transport of the Li^+ ions within the electrolyte between the particles of the composite electrode, transport of Li^+ across the electrode/electrolyte interface, diffusion of Li^+ within the intercalation host, electron transport from the current collector to the active electrode particles, and diffusion of electrons within the active particles. Any of these processes may be rate limiting. Reducing the dimensions of the electrode particles from the micrometer to the nanometer regime can enhance the rate.[1,2,24] The time constant for Li^+ and e^- insertion within the active particles is governed by the formula $\tau = L^2/2D$, where L is the diffusion length (the radius in the case of spherical particles) and D is the coupled diffusion coefficient for Li^+ and e^- (in most cases either the ions or electrons will be rate limiting in which case D will simplify to the diffusion coefficient of the slowest species). Since L is reduced on moving from micrometer-sized particles to those of nanodimensions, the time constant for diffusion is correspondingly lower. Smaller particles also increase the surface area facilitating Li^+ exchange across the electrode/electrolyte interface and generally lead to greater porosity between the particles aiding Li^+ transport through that portion of the electrolyte which lies within the electrode. In the case of two phase intercalation reactions, such as occurs with $LiFePO_4$, they are rendered more facile with small particles.[25−28]

For the above reasons, fabricating electrodes from nanoparticles has been the dominant approach taken to increase charge/discharge rates, but it is not without its problems. The small particles (low tap density) can make electrode fabrication more

(1) Arico, A. S.; Bruce, P.; Scrosati, B.; Tarascon, J. M.; Van Schalkwijk, W. *Nat. Mater.* **2005**, *4*, 366–377.
(2) Bruce, P. G.; Scrosati, B.; Tarascon, J. M. *Angew. Chem., Int. Ed.* **2008**, *47*, 2930–2946.
(3) Whittingham, M. S. *Chem. Rev.* **2004**, *104*, 4271–4301.
(4) Herle, P. S.; Ellis, B.; Coombs, N.; Nazar, L. F. *Nat. Mater.* **2004**, *3*, 147–152.
(5) Chen, H. L.; Grey, C. P. *Adv. Mater.* **2008**, *20*, 2206–2210.
(6) Taberna, L.; Mitra, S.; Poizot, P.; Simon, P.; Tarascon, J. M. *Nat. Mater.* **2006**, *5*, 567–573.
(7) Chung, S. Y.; Bloking, J. T.; Chiang, Y. M. *Nat. Mater.* **2002**, *1*, 123–128.
(8) Kang, B.; Ceder, G. *Nature* **2009**, *458*, 190–193.
(9) Dominko, R.; Bele, M.; Goupil, J. M.; Gaberscek, M.; Hanzel, D.; Arcon, I.; Jamnik, J. *Chem. Mater.* **2007**, *19*, 2960–2969.
(10) Luo, J. Y.; Zhang, J. J.; Xia, Y. Y. *Chem. Mater.* **2006**, *18*, 5618–5623.
(11) Long, J. W.; Swider-Lyons, K. E.; Stroud, R. M.; Rolison, D. R. *Electrochem. Solid State Lett.* **2000**, *3*, 453–456.
(12) Badway, F.; Cosandey, F.; Pereira, N.; Amatucci, G. G. *J. Electrochem. Soc.* **2003**, *150*, A1318–A1327.
(13) Yamada, A.; Koizumi, H.; Nishimura, S. I.; Sonoyama, N.; Kanno, R.; Yonemura, M.; Nakamura, T.; Kobayashi, Y. *Nat. Mater.* **2006**, *5*, 357–360.
(14) Meethong, N.; Huang, H. Y. S.; Speakman, S. A.; Carter, W. C.; Chiang, Y. M. *Adv. Funct. Mater.* **2007**, *17*, 1115–1123.
(15) Hu, Y. S.; Guo, Y. G.; Dominko, R.; Gaberscek, M.; Jamnik, J.; Maier, J. *Adv. Mater.* **2007**, *19*, 1963–1966.
(16) Cheng, F.; Tao, Z.; Liang, J.; Chen, J. *Chem. Mater.* **2008**, *20*, 667–681.
(17) Delmas, C.; Maccario, M.; Croguennec, L.; Le Cras, F.; Weill, F. *Nat. Mater.* **2008**, *7*, 665–671.
(18) Meethong, N.; Kao, Y. H.; Tang, M.; Huang, H. Y.; Carter, W. C.; Chiang, Y. M. *Chem. Mater.* **2008**, *20*, 6189–6198.
(19) Nishimura, S.; Kobayashi, G.; Ohoyama, K.; Kanno, R.; Yashima, M.; Yamada, A. *Nat. Mater.* **2008**, *7*, 707–711.
(20) Whittingham, M. S. *Dalton Trans.* **2008**, 5424–5431.
(21) Kobayashi, G.; Nishimura, S. I.; Park, M. S.; Kanno, R.; Yashima, M.; Ida, T.; Yamada, A. *Adv. Funct. Mater.* **2009**, *19*, 395–403.
(22) Lee, Y. J.; Yi, H.; Kim, W. J.; Kang, K.; Yun, D. S.; Strano, M. S.; Ceder, G.; Belcher, A. M. *Science* **2009**, *324*, 1051–1055.
(23) Sayle, T. X. T.; Maphanga, R. R.; Ngoepe, P. E.; Sayle, D. C. *J. Am. Chem. Soc.* **2009**, *131*, 6161–6173.
(24) Kavan, L.; Prochazka, J.; Spitler, T. M.; Kalbac, M.; Zukalova, M. T.; Drezen, T.; Gratzel, M. *J. Electrochem. Soc.* **2003**, *150*, A1000–A1007.

10.1021/ja905488x

difficult than for micrometer sized particles. The porosity between the particles is random in shape and size. Some pores will be too small for effective Li^+ transport and others larger than necessary thus wasting volume and compromising volumetric energy density more than is required in order to optimize rate (it is important to note that some lowering of the volumetric energy density of an electrode is an inevitable price to pay for achieving the highest rate capability). Maintaining electron pathways between the current collector and the active nanoparticles may be more difficult because there are many more contacts that must be preserved against a background of particles that are expanding and contracting on insertion/deinsertion. Such problems can lead to the need for more carbon, or carbon coating, to ensure that electron transport through the composite electrode is not rate limiting.

As an alternative to employing nanoparticles, mesoporous materials may be used. In this case, rather than reducing the particle dimensions of the active intercalation host from the micrometer to the nanoscale, the particles remain micrometer-sized but contain pores of nanometer dimensions separated by walls of similar size. This approach offers a number of advantages. Because the particles are of micrometer dimensions, fabrication into composite electrodes is similar to dense micrometer-sized particles, resulting in a similar packing density. The number of contacts that must be maintained between particles to ensure electron transport is not increased. The electrolyte can flood the pores leading to a high electrolyte/electrode contact area. The thin (nm-sized) walls ensure short diffusion distances for Li^+ on intercalation. In the case of ordered mesoporous materials, all the pores have the same dimensions (monodisperse), as do the walls, hence transport of Li^+ within the pores, and within the walls upon intercalation, is identical everywhere, and all of the surface is equally exposed to the electrolyte. Such monodispersity means that a pore size may be selected that is large enough to permit efficient Li^+ transport but without wasting volume on pores that are too large, unlike the random porosity between nanoparticles. In this way the inevitable reduction in volumetric energy density that accompanies the increased porosity needed to achieve the highest rates is mitigated as far as possible. The disadvantages of using a mesoporous intercalation host are that it may be more difficult to fabricate than nanoparticles and because the particles are of micrometer dimensions they do not enhance electron transport within the intercalation host. However, in general, mobility of electrons is far greater than ions in solids, so often ions will be rate limiting.

Composite electrodes containing ordered mesoporous intercalation hosts, e.g., mesoporous $LiMn_2O_4$ spinel, have been described and shown to exhibit superior rate performance and capacity retention on cycling, compared with bulk and nanoparticulate electrodes, thus demonstrating the potential advantages of mesoporous electrodes.[10,29−38] However, a fundamental understanding of how the critical dimensions of pore size and wall thickness control the rate capability of such an electrode is important in further evaluating the potential of mesoporous intercalation electrodes. Here we address this problem. We choose the mesoporous intercalation electrode β-MnO_2 to investigate the influence of the mesodimensions on rate capability for several reasons.[32] First, it is quite challenging to prepare a series of mesoporous intercalation electrodes of the same material that vary systematically in pore size and wall thickness while preserving the same highly crystalline structure within the walls, but this has proved possible for β-MnO_2. Second, it has been shown previously that intercalation of Li into mesoporous β-MnO_2 on the first discharge is associated with a two-phase intercalation reaction, whereas on subsequent cycling lithium intercalation occurs within a single phase.[32] Such duality allows us to investigate the influence of pore size and wall thickness on two-phase and single-phase intercalation processes within the same material.

Experimental Section

The mesoporous silica, KIT-6, was synthesized using different hydrothermal treatment temperatures (45, 60, 80, 100, and 120 °C) following the procedure described in previous reports.[39,40] A 10 g portion of the copolymer P123 surfactant was mixed with 349.4 mL of distilled water and 16 mL of concentrated HCl (36%). After stirring the mixture at 35 °C until homogeneous, 10 g of n-butanol (99.4%) was added, stirred for 1 h, and then combined with 21.5 g of tetraethyl orthosilicate (98%). After stirring at 35 °C for 24 h, the mixture was heated in an autoclave at 45, 60, 80, 100, or 120 °C for a further 24 h. The precipitate was filtered, dried at 60 °C, and then added to 300−400 mL of ethanol and 20−30 mL of concentrated HCl (36%). Following 1−2 h stirring, the mixture was filtered, washed several times with ethanol and water, and then dried at 60 °C. The resulting mesoporous solid was calcined at 500 °C for 3 h in air. The samples were denoted as KIT-45, KIT-60, KIT-80, KIT-100, and KIT-120, respectively, according to their hydrothermal treatment temperatures.

The preparation of disordered mesoporous silica with a pore diameter of ca. 8 nm was similar to the procedure for KIT-100, except that a different mole ratio of the reactants was used (0.017 P123/2.6 TEOS/2.6 BuOH/1.83 HCl/195 H_2O), such that the composition was located in the disordered region of the phase diagram.[40] A 10 g portion of the copolymer P123 surfactant was mixed with 349.4 mL of distilled water and 16 mL of concentrated HCl (36%). After stirring the mixture at 35 °C until homogeneous, 20 g of n-butanol (99.4%) was added, stirred for 1 h, and then combined with 55.9 g of tetraethyl orthosilicate (98%). Following stirring at 35 °C for 24 h, the mixture was heated in an autoclave at 100 °C for a further 24 h. The resulting mixture was filtered, dried at 60 °C, and then added to 300−400 mL of ethanol and 20−30 mL of concentrated HCl (36%). After 1−2 h of stirring, the mixture was filtered, washed several times with ethanol and water, and then dried at 60 °C. Following this procedure the resulting mesoporous solid was calcined at 500 °C for 3 h in air.

(25) Huang, H.; Yin, S. C.; Nazar, L. F. *Electrochem. Solid State Lett.* **2001**, *4*, A170–A172.
(26) Delacourt, C.; Poizot, P.; Levasseur, S.; Masquelier, C. *Electrochem. Solid State Lett.* **2006**, *9*, A352–A355.
(27) Wang, Y. G.; Wang, Y. R.; Hosono, E. J.; Wang, K. X.; Zhou, H. S. *Angew. Chem., Int. Ed.* **2008**, *47*, 7461–7465.
(28) Kim, D. H.; Kim, J. *Electrochem. Solid State Lett.* **2006**, *9*, A439–A442.
(29) Luo, J. Y.; Wang, Y. G.; Xiong, H. M.; Xia, Y. Y. *Chem. Mater.* **2007**, *19*, 4791–4795.
(30) Jiao, F.; Bao, J. L.; Hill, A. H.; Bruce, P. G. *Angew. Chem., Int. Ed.* **2008**, *47*, 9711–9716.
(31) Fan, J.; Wang, T.; Yu, C. Z.; Tu, B.; Jiang, Z. Y.; Zhao, D. Y. *Adv. Mater.* **2004**, *16*, 1432–1436.
(32) Jiao, F.; Bruce, P. G. *Adv. Mater.* **2007**, *19*, 657–660.
(33) Jiao, F.; Shaju, K. M.; Bruce, P. G. *Angew. Chem., Int. Ed.* **2005**, *44*, 6550–6553.
(34) Kim, H.; Cho, J. *J. Mater. Chem.* **2008**, *18*, 771–775.
(35) Lim, S. Y.; Yoon, C. S.; Cho, J. P. *Chem. Mater.* **2008**, *20*, 4560–4564.
(36) Zhou, H. S.; Li, D. L.; Hibino, M.; Honma, I. *Angew. Chem., Int. Ed.* **2005**, *44*, 797–802.
(37) Zhou, H. S.; Zhu, S. M.; Hibino, M.; Honma, I.; Ichihara, M. *Adv. Mater.* **2003**, *15*, 2107–2111.
(38) Ji, X. L.; Lee, K. T.; Nazar, L. F. *Nat. Mater.* **2009**, *8*, 500–506.
(39) Kleitz, F.; Choi, S. H.; Ryoo, R. *Chem. Commun.* **2003**, 2136–2137.
(40) Kim, T. W.; Kleitz, F.; Paul, B.; Ryoo, R. *J. Am. Chem. Soc.* **2005**, *127*, 7601–7610.

KIT-45, KIT-60, KIT-80, KIT-100, KIT-120, and the disordered ~8 nm mesoporous silica were used as the hard templates to prepare crystalline mesoporous β-MnO_2 following the procedure described in a previous report.[32] A 30 g portion of $Mn(NO_3)_2 \cdot 6H_2O$ (98%) was dissolved in 20 mL of water to form a saturated solution. A 5 g portion of mesoporous silica was dispersed in 200 mL of dried n-hexane. After stirring at room temperature for 3 h, 5 mL of the saturated $Mn(NO_3)_2$ solution was added slowly with stirring (for KIT-45, only 3.5 mL of saturated $Mn(NO_3)_2$ solution was added). The mixture was stirred overnight, filtered, and dried at room temperature until a completely dried powder was obtained. The sample was heated slowly to 400 °C at a rate of 1 °C/min and calcined at that temperature for 3 h, and after cooling to room temperature, the resulting material was treated twice with a 2 M hot NaOH solution, followed by washing with water several times and drying at 60 °C.

The preparation of ordered mesoporous β-MnO_2 with a relative high proportion of large pore (denoted as β-MnO_2-100B) followed a previously reported procedure.[41] A 4 g portion of $Mn(NO_3)_2 \cdot 6H_2O$ (98%) was dissolved in 150 mL of ethanol, followed by addition of 5 g of mesoporous silica, KIT-100. After stirring at room temperature until all the solution had been absorbed, the powder was redispersed in 100 mL of dry n-hexane under stirring in an open beaker. Once all the solvent had evaporated, the sample was heated slowly to 400 °C at a rate of 1 °C/min and calcined at that temperature for 3 h. After cooling to room temperature, the resulting sample was treated twice with a hot aqueous solution of 2 M NaOH to remove the silica template, followed by washing with water several times and then drying at 60 °C.

The preparation of disordered mesoporous β-MnO_2 with a pore diameter of ca. 30 nm was as follows: 100 g of Ludox AS-40 colloid silica (40%) was first dried at 60 °C overnight, then impregnated with 10 mL of saturated $Mn(NO_3)_2$ solution and again dried. Following this procedure it was calcined at 400 °C for 3 h. Finally, the resulting material was treated twice with a 2 M hot NaOH solution, followed by washing with water several times and drying at 60 °C.

TEM studies were carried out using a JEOL JEM-2011, employing a LaB6 filament as the electron source and an accelerating voltage of 200 keV. TEM images were recorded by a Gatan CCD camera in a digital format. Wide-angle powder X-ray diffraction data were collected on a Stoe STADI/P powder diffractometer operating in transmission mode and with a small angle position sensitive detector. Incident radiation was generated using a Fe Kα1 source (λ = 1.936 Å). Low-angle powder X-ray diffraction data were collected using a Rigaku/MSC, D/max-rB with Cu Kα_1 radiation (λ = 1.541 Å) operating in reflection mode with a scintillation detector. N_2 adsorption−desorption analysis was carried out using a Micromeritics ASAP 2020. The typical sample weight used was 100−200 mg. The outgas condition was set to 180 min at 120 °C under vacuum, and all adsorption−desorption measurements were carried out at liquid nitrogen temperature.

Electrochemical cells were constructed by mixing the active material, Kynar 2801 (a copolymer based on polyvinylidene fluoride), and Super S carbon (MMM) in the weight ratio 70:15:15, unless stated otherwise. The mixture was cast onto Al foil (99.5%, thickness 0.050 mm, Advent Research Materials, Ltd.) from acetone using a Doctor-Blade technique. After solvent evaporation at room temperature and heating at 80 °C under vacuum for 8 h, the electrodes were assembled into cells (the cathode and anode diameter was 13 mm) with a Li electrode and LP 30 electrolyte (Merck; 1 M $LiPF_6$ in 1:1 v/v ethylene carbonate/dimethyl carbonate). The cells were constructed and handled in an Ar-filled MBraun glovebox. Electrochemical measurements were carried out at 30 °C using a MACCOR series 4200 cycler.

Samples for neutron diffraction were prepared electrochemically at a rate of 10 mA/g at 30 °C. After the first discharge, cells were transferred to an argon-filled glovebox before opening and removing the active material. The electrodes were rinsed with a small amount of dry solvent (DMC) to remove residual electrolyte. They were then left under dynamic vacuum overnight to ensure all solvent had evaporated. The samples were then transferred to 2 mm quartz capillaries.

The structures of the materials were characterized using neutron diffraction. Time-of-flight powder neutron diffraction data were collected on both the GEM and Polaris high intensity, medium-resolution instruments at ISIS, Rutherford Appleton Laboratory. The structures were refined by the Rietveld method using the program TOPAS Academic.[42]

Results and Discussion

First the control of pore size/wall thickness and characterization of the mesoporous materials will be described, followed by the structure of the lithium intercalated, Li_xMnO_2-β, phase, and then the electrochemical behavior associated with the two-phase and single-phase intercalation will be discussed.

Control of Pore Size/Wall Thickness. Ordered mesoporous β-MnO_2 was synthesized using the ordered mesoporous silica, KIT-6, as a hard template, because the high processing temperatures compared with soft templates ensures the combination of an ordered pore structure and highly crystalline walls that is desirable for intercalation. KIT-6 possesses a 3D pore structure that results in a mesoporous β-MnO_2 with a replica 3D pore architecture.[32] The pore size of KIT-6 was varied by altering the hydrothermal conditions used during the synthesis.[39,40] Since the pores of the silica template become the walls of the mesoporous β-MnO_2, it is possible to obtain a range of wall thicknesses for the latter. It is difficult to vary continuously the pore size in mesoporous β-MnO_2. However, it is possible to prepare mesoporous β-MnO_2 with a bimodal pore size distribution and to vary the ratio of the two pore sizes and in this way explore the influence of pore size on rate. KIT-6 contains two set of mesopores connected by microporous channels.[39,40,43] The prevalence of these channels varies with the hydrothermal synthesis conditions. A large number of microporous channels ensures complete filling of both sets of mesopores resulting, on casting, in mesoporous β-MnO_2 with pores of ~3.4 nm diameter, whereas fewer microporous channels, along with the use of a lower ratio of $Mn(NO_3)_2$ to KIT-6, result in a mesoporous β-MnO_2 with 11 nm diameter pores.[41,44,45] A more detailed explanation of how different pore sizes may be generated is given in the cited references.[41,45,46] Generally, bimodal pore size distributions are obtained (i.e., 3.4 and 11 nm diameter pores coexist). In this way, mesoporous β-MnO_2 with different proportions of large (ca. 11 nm) to small (ca. 3.4 nm) diameter pores may be prepared. The degree to which the pore size and wall thickness can be varied while preserving the highly ordered mesostructure is restricted. Therefore, to explore thicker walls and larger pores we synthesized two mesoporous β-MnO_2 materials with disordered pore structures. The first uses a silica template synthesized by the same method as KIT-6, but employing different mole ratios of reactants that take the solution composition outside the ordered regime.[40] The second

(41) Jiao, F.; Hill, A. H.; Harrison, A.; Berko, A.; Chadwick, A. V.; Bruce, P. G. *J. Am. Chem. Soc.* **2008**, *130*, 5262–5266.
(42) Coelho, A. A. *J. Appl. Crystallogr.* **2000**, *33*, 899–908.
(43) Sakamoto, Y.; Kim, T. W.; Ryoo, R.; Terasaki, O. *Angew. Chem., Int. Ed.* **2004**, *43*, 5231–5234.
(44) Jiao, K.; Zhang, B.; Yue, B.; Ren, Y.; Liu, S. X.; Yan, S. R.; Dickinson, C.; Zhou, W. Z.; He, H. Y. *Chem. Commun.* **2005**, 5618–5620.
(45) Rumplecker, A.; Kleitz, F.; Salabas, E. L.; Schuth, F. *Chem. Mater.* **2007**, *19*, 485–496.
(46) Dickinson, C.; Zhou, W. Z.; Hodgkins, R. P.; Shi, Y. F.; Zhao, D. Y.; He, H. Y. *Chem. Mater.* **2006**, *18*, 3088–3095.

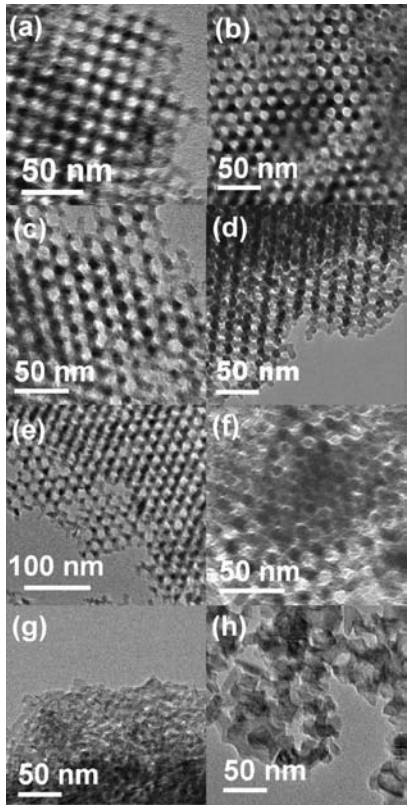

Figure 1. TEM images of different crystalline mesoporous β-MnO_2 materials: (a) β-MnO_2-45, (b) β-MnO_2-60, (c) β-MnO_2-80, (d) β-MnO_2-100, (e) β-MnO_2-100B, (f) β-MnO_2-120, (g) β-MnO_2-d4, and (h) β-MnO_2-d30.

employed colloid silica beads (~30 nm) that self-assemble to form a mesoporous structure (see Experimental Section for details).

The following nomenclature was used to describe the various mesoporous β-MnO_2 materials: β-MnO_2-45, -60, -80, -100, -120, templated from KIT-6 synthesized using the corresponding hydrothermal temperatures. β-MnO_2-100B, templated from KIT-6 synthesized at 100 °C but with a lower proportion of β-MnO_2 precursor to KIT-6 ratio than β-MnO_2-100. β-MnO_2-d4 and β-MnO_2-d30 correspond to the two disordered materials with average pore dimensions of 4 and 30 nm, respectively.

TEM images for the various mesoporous materials are shown in Figure 1. The porosity is clearly evident, and examination of many particles demonstrated that the mesoporosity is replicated throughout the materials. Low and wide angle powder X-ray diffraction data for all the materials are presented in Figure 2. The mesoporous materials from β-MnO_2-45 through -120 all exhibit a well-defined low angle peak at around 1° in 2θ, consistent with the well-ordered pore structures evident in Figure 1a−f. The peak in Figure 2a corresponds to the 211 reflection of the *Ia3d* space group anticipated for the replica structure of KIT-6. The a_0 lattice parameters for the mesostructures obtained from the low angle PXRD data are presented in Table 1.

Although β-MnO_2-d4 is designated as disordered, a small peak is evident in the low-angle PXRD indicating a degree of order.[47] From the wide-angle PXRD data, Figure 2b, it is clear that all the mesoporous materials possess the same β-MnO_2 crystal structure, although of course the peaks are broadened

(47) Tanev, P. T.; Pinnavaia, T. J. *Science* **1995**, *267*, 865–867.

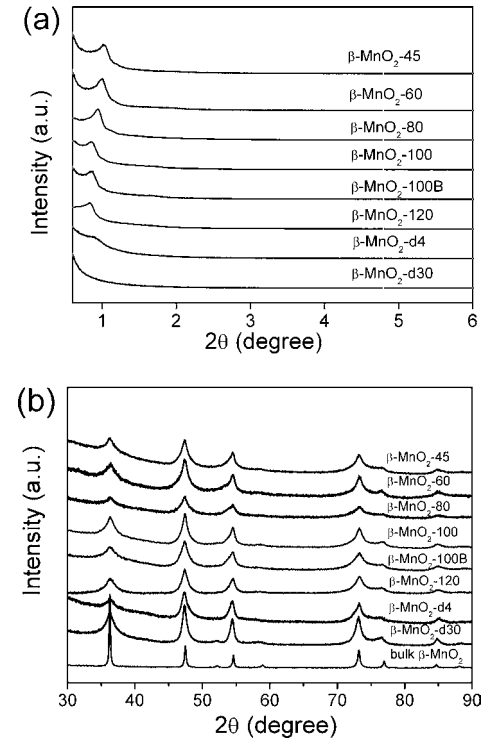

Figure 2. (a) Low-angle and (b) wide-angle PXRD patterns of different crystalline mesoporous β-MnO_2 materials.

Table 1. Physicochemical Properties of the Mesoporous β-MnO_2 Materials[a]

materials	a_0 (nm)	S_{BET} (m^2/g)	D (nm)	V (cm^3/g)	pore wall thickness (nm, by TEM)
β-MnO_2-45	21.0	123	3.5/11.2 (0.46)	0.48	4.7
β-MnO_2-60	21.6	133	3.4/11.0 (0.06)	0.24	5.0
β-MnO_2-80	23.0	124	3.3/11.0 (0.14)	0.24	6.5
β-MnO_2-100	25.2	121	3.4/11.1 (0.14)	0.26	7.5
β-MnO_2-120	25.9	99	3.5	0.25	8.5
β-MnO_2-100B	25.0	87	3.3/11.1 (0.26)	0.23	7.5
β-MnO_2-d4	24.7	120	3.4/5.0 (0.45)	0.25	8−10
β-MnO_2-d30		35	28	0.24	20−30

[a] a_0, the unit cell parameters obtained from the low-angle PXRD data; S_{BET}, surface area calculated by the BET method; D, pore diameter calculated by the BJH method [ratios of large (11 or 5 nm) to small (3.4 nm) pore volumes are given in parentheses]; V, total pore volume at $P/P_0 = 0.99$.

compared with bulk β-MnO_2 in keeping with the small dimensions of the mesoporous walls.

The pore structures were investigated further by nitrogen sorption measurements (Figure 3). These data exhibit a typical type IV isotherm with a H_2 hysteresis loop, as expected for such mesoporous metal oxides.[44,48−54] The BET surface areas, pore

(48) Sing, K. S. W.; Everett, D. H.; Haul, R. A. W.; Moscou, L.; Pierotti, R. A.; Rouquerol, J.; Siemieniewska, T. *Pure Appl. Chem.* **1985**, *57*, 603–619.
(49) Zhu, K. K.; Yue, B.; Zhou, W. Z.; He, H. Y. *Chem. Commun.* **2003**, 98–99.
(50) Laha, S. C.; Ryoo, R. *Chem. Commun.* **2003**, 2138–2139.
(51) Tian, B. Z.; Liu, X. Y.; Yang, H. F.; Xie, S. H.; Yu, C. Z.; Tu, B.; Zhao, D. Y. *Adv. Mater.* **2003**, *15*, 1370–1374.
(52) Tian, B. Z.; Liu, X. Y.; Solovyov, L. A.; Liu, Z.; Yang, H. F.; Zhang, Z. D.; Xie, S. H.; Zhang, F. Q.; Tu, B.; Yu, C. Z.; Terasaki, O.; Zhao, D. Y. *J. Am. Chem. Soc.* **2004**, *126*, 865–875.
(53) Wang, Y. Q.; Yang, C. M.; Schmidt, W.; Spliethoff, B.; Bill, E.; Schüth, F. *Adv. Mater.* **2005**, *17*, 53–56.

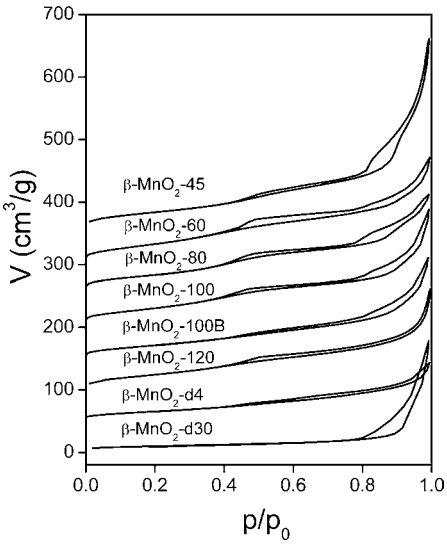

Figure 3. N_2 adsorption−desorption isotherms for the crystalline mesoporous β-MnO_2 materials. The isotherms for β-MnO_2-45, β-MnO_2-60, β-MnO_2-80, β-MnO_2-100, β-MnO_2-100B, β-MnO_2-120, β-MnO_2-d4, and β-MnO_2-d30 are offset vertically by 350, 300, 250, 200, 150, 100, 50, and 0 cm^3/g, respectively.

sizes (determined by the BJH method), pore volumes and wall thicknesses are presented in Table 1. The relative proportions of the two sets of pores were obtained from the peak areas in the pore size distribution plot (Figure S1). The pore volumes are similar for all the materials except β-MnO_2-45. Considering first the four mesopores, β-MnO_2-60, -80, -100, and -120, the pore wall thickness increases systematically from 5.0 to 8.5 nm on increasing the hydrothermal synthesis temperature. The pore sizes for all four mesopores are invariant, but the proportion of the larger (11 nm pores) is very small (6% and 0%) for β-MnO_2-60 and -120, rising to 14% for β-MnO_2-80 and -100. β-MnO_2-100B possesses the same wall thickness and pore size as β-MnO_2-100, but the proportion of larger (11 nm pores) has increased substantially to 26% and the surface area has decreased, thus offering a very direct comparison of how such factors influence the performance. As can be seen from Table 1, the two disordered materials exhibit thicker walls, 8−10 and 20−30 nm for β-MnO_2-d4 and d30, respectively. Although the larger pore in β-MnO_2-d4 (5 nm) is smaller than those in ordered materials (11 nm), the proportion of the larger pores in β-MnO_2-d4 is significantly high at 45%. β-MnO_2-d30 possesses a large pore size of ∼28 nm diameter. Of course with these disordered materials pore size distributions are inevitably broader than in the highly ordered materials.

Structure of Mesoporous Li_xMnO_2-β. On intercalating lithium into mesoporous β-MnO_2, the material transforms from the tetragonal rutile structure (space group $P4_2/mnm$) to a new phase, mesoporous Li_xMnO_2-β with orthorhombic symmetry (space group *Pnnm*). Note that the previous report of this transformation assigned a tetragonal space group to Li_xMnO_2-β, as a result of the poor quality of the powder X-ray diffraction data.[32] The powder neutron diffraction pattern for the Li_xMnO_2-β phase exhibits very broad peaks (Figure 4a), to an extent that precludes direct structure elucidation. Recently we have investigated lithium intercalation into β-MnO_2 nanowires with a diameter of approximately 50 nm. The powder neutron diffraction pattern

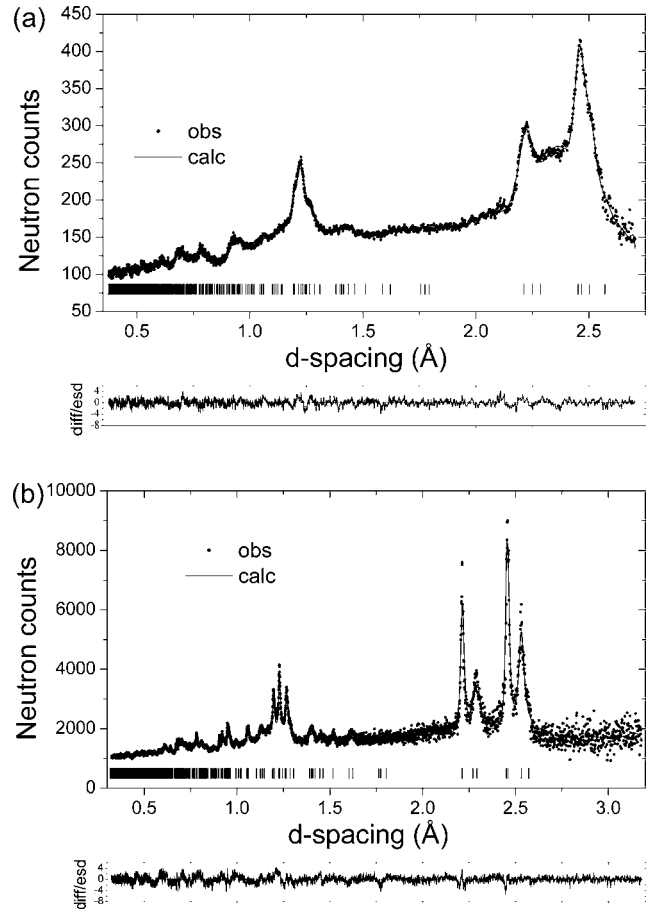

Figure 4. Refined powder neutron diffraction patterns for (a) mesoporous Li_xMnO_2-β-100 and (b) Li_xMnO_2-β nanowires. Dots represent observed data, and the solid line represents the calculated pattern. The lower line is the difference/esd. Tick marks represent allowed reflections.

is shown in Figure 4b. Comparison of parts a and b of Figure 4 demonstrate significant structural similarity. Both patterns may be indexed on the same orthorhombic unit cell, but because the diameter of the wires is much greater than the thickness of the walls in mesoporous β-MnO_2 (∼8 nm), the peaks in the neutron powder pattern of the Li_xMnO_2-β nanowires are sharper and hence better resolved (Figure 4b). By first elucidating the structure of the Li_xMnO_2-β nanowires, it has been possible to establish the structure of lithium intercalated mesoporous β-MnO_2. Structure elucidation of the Li_xMnO_2-β nanowires is described in detail elsewhere and is based on refinement starting from Li_xRuO_2.[55,56] Using the structure obtained for the lithium intercalated nanowires, Rietveld refinement was carried out on the Li_xMnO_2-β mesoporous phase, resulting in the structure shown in Figure 5b and detailed in Table 2. The fit is good, as is reflected in a R_{wp} of 2.4% (R_{exp} = 2.1%). The structure of mesoporous orthorhombic Li_xMnO_2-β is in essence a significantly distorted form of the tetragonal rutile structure with Li^+ ions in the tunnels (Figure 5). Comparison of the lattice parameters of the parent phase with those for mesoporous Li_xMnO_2-β shows that a very large anisotropic cell expansion occurs on lithium intercalation. The *a* parameter expands by almost 16.7%, and *b* by 13.5%, while the *c* parameter actually contracts by 2%. The *c* direction lies along the 1 × 1 tunnels

(54) Ren, Y.; Ma, Z.; Qian, L. P.; Dai, S.; He, H.; Bruce, P. G. *Catal. Lett.* **2009**, *131*, 146–154.
(55) Davidson, I. J.; Greedan, J. E. *J. Solid State Chem.* **1984**, *51*, 104–117.
(56) Armstrong, A. R.; Bruce, P. G. private communication.

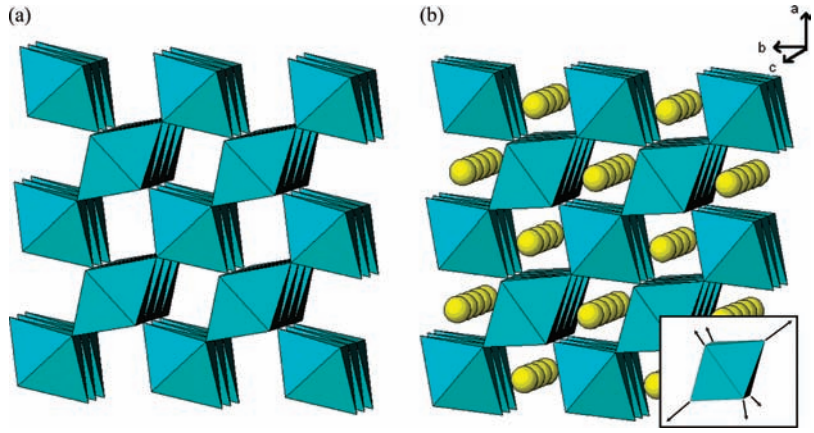

Figure 5. Crystal structures of (a) β-MnO_2 and (b) Li_xMnO_2-β viewed down the 1 × 1 tunnels. Inset shows the distortion of the MnO_6 octahedra on intercalation.

Table 2. Refined Crystallographic Parameters for Mesoporous Li_xMnO_2-β-100 at the End of the First Discharge[a]

atom	Wyckoff symbol	x/a	y/b	z/c	B_{iso}	occupancy
Mn	2a	0.0	0.0	0.0	0.8(2)	1
O1	4g	0.277(3)	0.3218(14)	0.0	0.40(7)	1
Li1	2d	0.0	0.5	0.5	0.5(−)	0.99(12)

[a] R_e = 2.1%, R_{wp} = 2.4%, R_p = 2.1%. Space group *Pnnm*. a = 5.141(7) Å, b = 5.003(2) Å, c = 2.8131(8) Å.

with a and b perpendicular to the tunnel axis. The large increase in a and b corresponds to a significant increase in the width of the 1 × 1 tunnel in order to accommodate the Li^+ ions, which are located in the octahedral sites. The MnO framework is clearly similar to the parent rutile structure, but the MnO_6 octahedra are enlarged and distorted, with elongated apical bonds, consistent with Jahn−Teller active Mn^{3+} (MnO_6 distortion shown in Figure 5). The elongation of the MnO_6 octahedra occurs along the [110] direction in the *ab* plane and is in accord with the expansion of 1 × 1 tunnels.

Electrochemical Behavior. Composite electrodes composed of the various mesoporous materials, carbon, and binder were fabricated as described in the Experimental Section. Since our primary interest is to understand how the mesodimensions of the mesoporous electrodes influence the rate capability, it is important to establish first that the observed electrochemical behavior is limited by these factors, rather than by lithium ion transport between the particles or electron transport to the particles. It has been known for decades that, especially at high rates, the transport of lithium within the electrolyte inside the composite electrode can be rate limiting.[57−61] Such transport may be confused with diffusion inside the particles. To ensure that the electrode thickness and current densities used here are within a range such that the rate is not limited by transport in the electrolyte, β-MnO_2-100B electrodes were prepared with various electrode thicknesses (loadings). Their discharge capacities are shown in Figure 6 for two different rates, 600 and 1500 mA/g. At the highest rate, the highest loading is associated with a lower capacity; therefore, a loading of 2.5 mg/cm^2 was chosen in order to investigate the effect of mesoporous dimensions on rates up to 1500 mA/g. To ensure that the rate performance was not limited by electron transport to the particles, three different β-MnO_2-100B-based electrodes containing increasing proportions of carbon were investigated, Figure 7. At the highest rate used, 1500 mA/g, a carbon content of at least 15% was necessary to ensure that the discharge capacity was not limited by electron transport to the particles. This composite electrode composition was used throughout the remaining studies.

The variation of load potential with state-of-charge for the first and tenth cycles of mesoporous β-MnO_2 is shown in Figure 8. The first discharge exhibits a well-defined plateau associated with the two-phase intercalation process between β-MnO_2 and Li_xMnO_2-β. After cycling, the load curve shows a continuous variation of potential with state of charge, in accord with the known single-phase intercalation process associated with Li_xMnO_2-β.[32] In the following two subsections we consider, in turn, how the mesodimensions influence the one- and two-phase intercalation processes.

Influence of Mesodimensions on the Two-Phase Intercalation Reaction (First Discharge of β-MnO_2). The discharge rate capability of each mesoporous β-MnO_2 material on first discharge is demonstrated by plotting the variation of the first discharge capacity as a function of current density (rate). These data are presented in Figure 9. The better the capacity retention with increasing the current density, the better the discharge rate capability of the material. The absolute capacities at low rates differ for different mesopores (we shall return to this point later); hence, the data are presented as a percentage of the discharge capacity at the lowest rate (15 mA/g) to facilitate comparison of the rate capabilities for different mesoporous materials. Considering first the four materials, mesoporous β-MnO_2-60, -80, -100, and -120, which differ principally in their wall thickness, it is evident that the rate capability decreases with increasing pore wall thickness from 5 to 8.5 nm, i.e., an increase in wall thickness of 70%.

Comparing the rate capability of β-MnO_2-100B and β-MnO_2-100, the capacity retention of the former is clearly superior to the latter. The wall thickness is the same in both cases, 7.5 nm; therefore, the origin of the difference must lie in the pore size. β-MnO_2-100B possesses a significantly higher proportion of the larger, 11 nm, pores, 26% versus 14%. This demonstrates that, for pore sizes and wall thicknesses within the range studied in this work, both parameters play an important role in determining

(57) Thurston, C. G.; Owen, J. R.; Hargreaves, N. J. *J. Power Sources* **1992**, *39*, 215–224.
(58) Atlung, S.; West, K.; Jacobsen, T. *J. Electrochem. Soc.* **1979**, *126*, 1311–1321.
(59) West, K.; Jacobsen, T.; Atlung, S. *J. Electrochem. Soc.* **1982**, *129*, 1480–1485.
(60) Atlung, S.; West, K. *J. Power Sources* **1989**, *26*, 139–159.
(61) Johns, P. A.; Roberts, M. R.; Wakizaka, Y.; Sanders, J. H.; Owen, J. R. *Electrochem. Commun.* **2009**, *11*, 2089–2092.

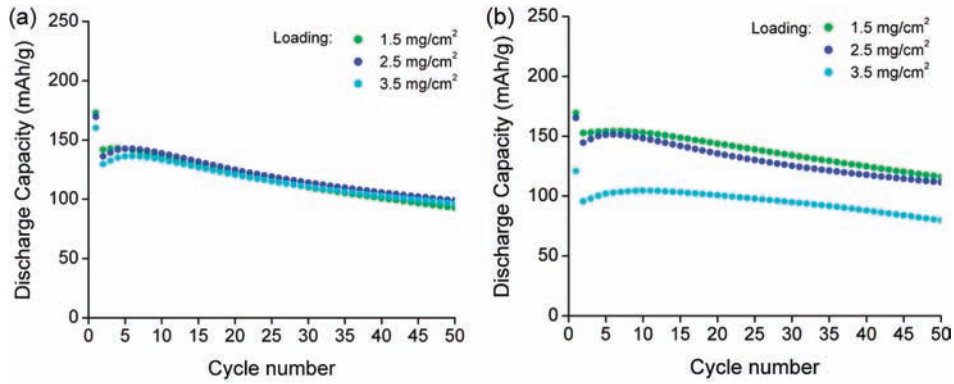

Figure 6. Variation of the discharge capacity with cycle number for composite electrodes containing mesoporous β-MnO_2-100B, Super S carbon, and Kyner 2801, with weight ratios of 70:15:15 and with three different β-MnO_2 mass loadings, at rates of (a) 600 mA/g and (b) 1500 mA/g.

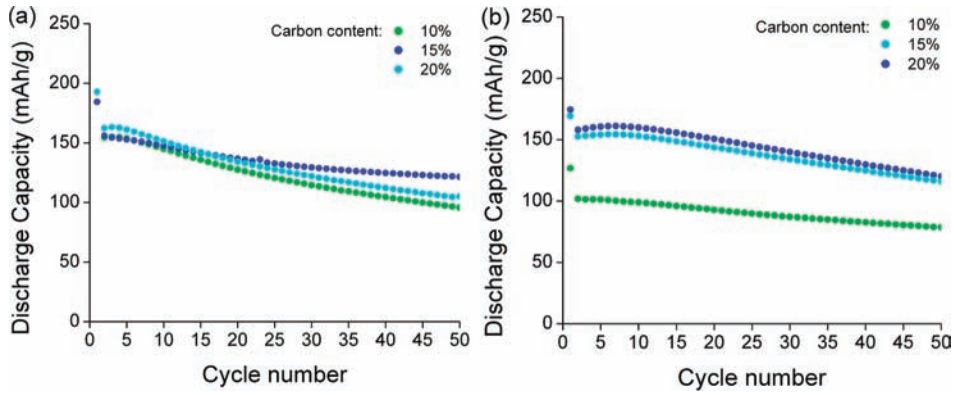

Figure 7. Variation of the discharge capacity with cycle number for composite electrodes containing mesoporous β-MnO_2-100B, Super S carbon, and Kyner 2801 with the three different weight ratios (green 80:10:10, blue 70:15:15, cyan 70:20:10) at rates of (a) 300 mA/g and (b) 1500 mA/g. The active material mass loading is 2.5 mg/cm^2.

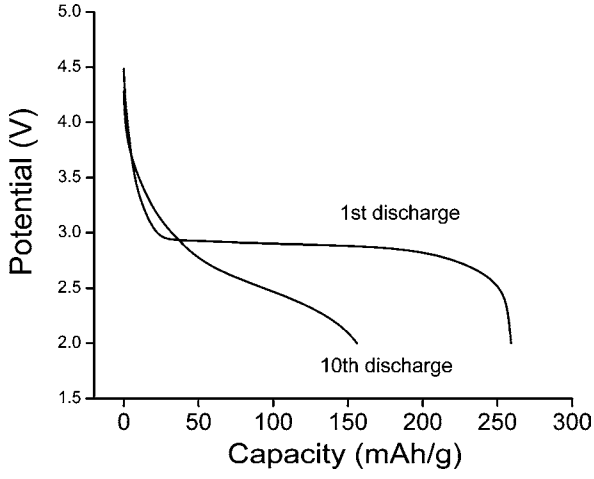

Figure 8. Typical variation of potential with state of charge (load curves) for the first and tenth discharges of mesoporous β-MnO_2.

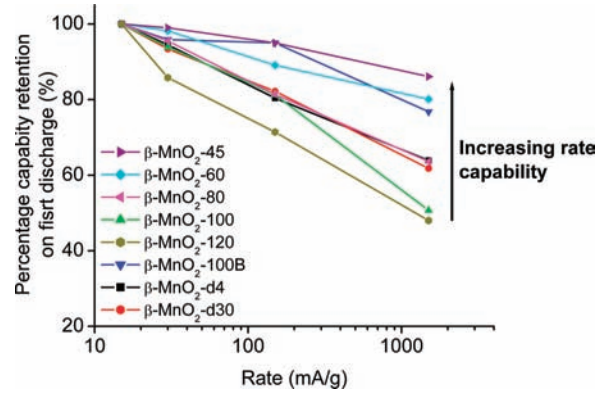

Figure 9. First discharge capacity for different mesoporous β-MnO_2 electrodes as a function of rate. Note the capacity is expressed as a percentage of the discharge capacity at the lowest rate (15 mA/g). The active material mass loading is 2.5 mg/cm^2.

the rate. The significance of the pore size is further reinforced by comparing β-MnO_2-45 and β-MnO_2-60; there is only a small difference in wall thickness (4.7 and 5 nm, respectively), but the latter has a much higher proportion of 11 nm pores (46% vs 6% for β-MnO_2-60). β-MnO_2-45 exhibits better rate performance than β-MnO_2-60.

Comparing the rate capability of the disordered materials with those just discussed, β-MnO_2-d4 has a greater wall thickness than β-MnO_2-100 and β-MnO_2-100B, yet its rate capability lies between the two 100 materials; this must be an effect of the pore sizes. Although β-MnO_2-d4 does not have 11 nm pores, it does have a higher proportion of 5 nm pores (45%) compared with the proportion of 11 nm pores in either β-MnO_2-100 (14%) or β-MnO_2-100B (26%). It appears that such a large proportion of 5 nm pores is sufficient to raise the rate capability of β-MnO_2-d4 above that of β-MnO_2-100 but not β-MnO_2-100B. Finally, β-MnO_2-d30 has thick walls, 20−30 nm, and therefore should have the poorest rate performance. However, it also has the largest pores, ~28 nm, which places its rate capability between β-MnO_2-100 and β-MnO_2-100B.

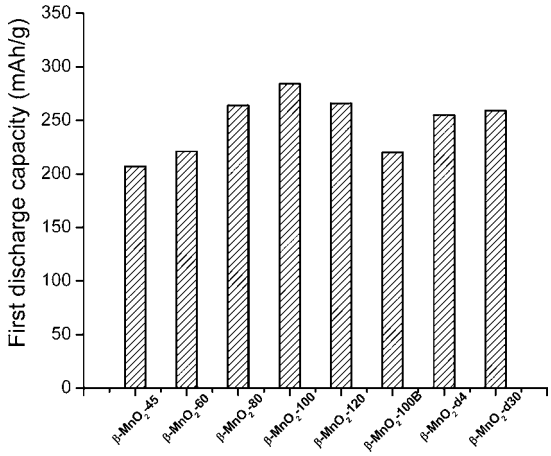

Figure 10. First discharge capacities at 15 mA/g for different mesoporous β-MnO_2.

Considering the influence of pore size on rate, an increase in rate capability with increasing pore diameter is consistent with the expectation that larger pores permit more facile Li^+ transport in the electrolyte within the pores. The data presented here show that varying the pore size between 5 and 30 nm has a significant effect on the rate capability for current densities in the range 100−1500 mAh/g.

Considering the influence of wall thickness on rate, it is known that, for two-phase intercalation reactions, such as in $LiFePO_4$, nanoparticles exhibit significantly higher rate capability than micrometer-sized particles.[14,25−28] Recent work has attributed this to a change in the intercalation mechanism from one in which the new phase, in this case $FePO_4$, nucleates and grows through the $LiFePO_4$ particle when of micrometer dimensions[62] to one in which either $LiFePO_4$ or $FePO_4$, but not both, is present within a single particle.[17] In the case of mesoporous electrodes, the walls are of nanometer dimensions, but the particles are micrometer-sized; hence, an entire particle cannot convert from one phase to another, and phase boundaries must remain. The results presented here show that the thin walls can accommodate the strain of the phase boundary between β-MnO_2 and Li_xMnO_2-β despite the large volume expansion on intercalation (55.7−72.3 Å^3) and its significant anisotropy ($a = 4.406$ Å, $c = 2.868$ Å for the β-MnO_2; and $a = 5.141$ Å, $b = 5.002$ Å, $c = 2.813$ Å for Li_xMnO_2-β). For this reason, despite the particle size being of micrometer dimensions, the intercalation process is rendered far more facile than that for dense micrometer-sized materials.

First Discharge Capacity at Low Rates. In order to compare the discharge rate capabilities of different mesoporous β-MnO_2 materials, the capacities in Figure 9 were expressed as a percentage of their capacity at the lowest rate (15 mA/g), because the low rate capacities differ from one mesoporous β-MnO_2 to another. The first discharge capacities at 15 mA/g for each mesopore are presented in Figure 10. Considering the four mesoporous materials β-MnO_2-45, β-MnO_2-60, β-MnO_2-80, and β-MnO_2-100, it is clear that the discharge capacity increases with increasing wall thickness. This is counter to what would be expected if the capacities were limited by kinetics. We have observed similar behavior in other mesoporous materials, specifically mesoporous β-MnO_2 with a 1D pore structure prepared from SBA-15, for which capacities increased from 225 mAh/g (wall thickness 7.5 nm) to 265 mAh/g (wall thickness 10.1 nm) at 15 mA/g.[63] We cannot be certain of the origin of this effect but offer the following hypothesis. We propose that the explanation lies in the relative proportion of "bulk" and "near surface" regions within the walls of the mesoporous solids and that the latter is a poor host for Li. At the center of the walls of the mesoporous solid, farthest from the pores, Figure S2, the structure will be that of undistorted bulk β-MnO_2. Progressing from this region toward the pores, Figure S2, it is possible that the crystal structure will become increasingly distorted. This could arise from the severe curvature of the walls of the small (nm) pores. Recently, we have studied a different nanomaterial, TiO_2(B) nanotubes.[64−66] The nanotube is composed of thin walls formed by folding a 2.5 nm slab of the TiO_2(B) crystal structure to form a tube of internal diameter 5 nm. We have shown that this curvature induces severe distortions of the regular TiO_2(B) crystal structure.[66] However, in the case of TiO_2(B) nanotubes the distorted structure results in an increased capacity to store Li, whereas here the opposite must be true. It should be recalled that the mesporous materials are grown within a silica template, the walls of which are disordered and form interfaces with what becomes the pore surfaces of β-MnO_2 on template removal. This could induce disorder in the β-MnO_2 walls close to the pore surfaces. The thinnest pore walls are found for β-MnO_2-45 (4.7 nm) with the pore wall thickness increasing by 50% in the case of β-MnO_2-100. Therefore, the proportion of distorted "near-surface" structure compared with "bulk" structure will be greatest for β-MnO_2-45. If the distorted structure is less able to accommodate lithium than the undistorted (bulk) structure, then the highest capacity will be found in the mesopore with thickest walls, i.e., in β-MnO_2-100, in accord with observation (Figure 10).

A further increase in wall thickness does not increase the capacity, as demonstrated by β-MnO_2-d4 and β-MnO_2-d30. This may be attributed to the fact that as the walls become thicker the proportion of undistorted structure dominates, and hence, the capacity saturates. Finally, we must consider the cases of β-MnO_2-100B and β-MnO_2-120: the former exhibits a lower first discharge capacity than β-MnO_2-100 with the same wall thickness and the latter a lower capacity despite thicker walls. The common factor is both have significantly lower surface areas than β-MnO_2-100 (Table 1). Why should the reduction in surface area reduce the capacity of the material? When lithium is inserted into β-MnO_2, the lithium-rich phase will nucleate and grow at a variety of points scattered across the pore wall surfaces. We speculate that the lower surface areas of β-MnO_2-100B and β-MnO_2-120 will result in fewer nuclei from which the new phase grows and, even at this low rate, greater polarization will occur. However, this hypothesis requires further examination in future work.

Influence of Mesodimensions on the Single Phase Intercalation Reaction (Tenth Discharge of β-MnO_2). Turning to the influence of pore size and wall thickness on the rate of lithium intercalation for a single phase reaction, i.e., at high cycle

(62) Chen, G. Y.; Song, X. Y.; Richardson, T. J. *Electrochem. Solid State Lett.* **2006**, *9*, A295–A298.
(63) Ren, Y.; Armstrong, A. R.; Jiao, F.; Bruce, P. G. In preparation.
(64) Armstrong, G.; Armstrong, A. R.; Canales, J.; Bruce, P. G. *Chem. Commun.* **2005**, 2454–2456.
(65) Armstrong, G.; Armstrong, A. R.; Canales, J.; Bruce, P. G. *Electrochem. Solid State Lett.* **2006**, *9*, A139–A143.
(66) Andreev, Y. G.; Bruce, P. G. *J. Am. Chem. Soc.* **2008**, *130*, 9931–9934.

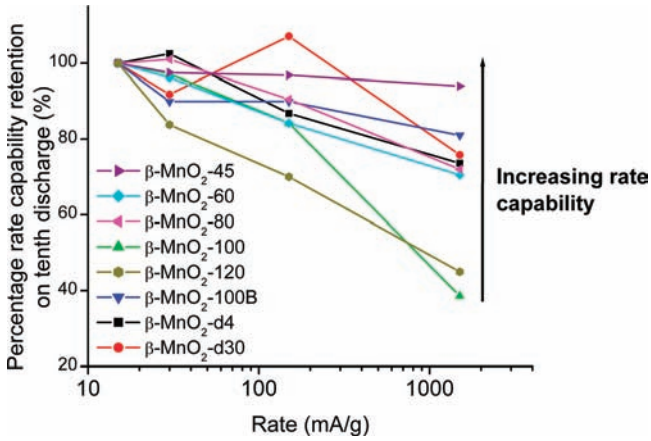

Figure 11. Tenth discharge capacities for the different mesoporous β-MnO_2 electrodes at different rates as a percentage of the discharge capacity at the lowest rate (15 mA/g). The active materials mass loading is 2.5 mg/cm^2.

numbers within the mesoporous Li_xMnO_2-β phase, the discharge capacity retention with increasing rate for cycle 10 is shown in Figure 11. The data demonstrate that at the extremities of the range of pore size/wall thickness explored in this work, i.e., for β-MnO_2-45 (which combines the thinnest walls, 4.7 nm, with a high proportion, 46%, of large, 11 nm, pores) and β-MnO_2-120 (combining relatively thick walls, 8.5 nm, with 100% of 3.5 nm pores), pore size and wall thickness influence the rate performance. However, it is interesting to note that the rest of the materials studied here, except β-MnO_2-100 at the very highest current density (1500 mA/g), show little variation of rate capability with variation of pore size and wall thickness.

Comparing lithium intercalation into β-MnO_2, via a single phase mechanism with that via a two-phase process, it is clear that the latter is sensitive to variations in both pore size and wall thickness, whereas the former is insensitive to such variations except for the more extreme combinations of pore size and wall thickness studied here. Of course, the range of pore size and wall thickness reported here is limited and restricted to one system β-MnO_2; therefore, the observed trends should be considered in that context. Nevertheless, they do offer a valuable guide to the effect of mesoporous morphology on electrode performance.

Conclusions

By preparing a series of electrodes based on mesoporous β-MnO_2 as the intercalation host, with pore sizes ranging from 3.4 to 28 nm in diameter, and wall thicknesses from 4.7 to 30 nm, it has been possible to explore the influence of pore size and wall thickness on the rate of intercalation. The rate capabilities of both one- and two-phase intercalation processes have been investigated by examining the first discharge (two phase) and 10th discharge (single phase) behavior, permitting comparison of the influence of the pore size/wall thickness between the two mechanisms. The pore size and wall thickness have a significant effect on the rate of lithium intercalation via single phase and two-phase mechanisms. However, the former requires more extreme variation in pore size/wall thickness to promote a change in rate than the latter.

Acknowledgment. Y.R. thanks EaStCHEM for a studentship. P.G.B. is indebted to the EPSRC, including the SUPERGEN program, and the EU for financial support.

Supporting Information Available: Additional supporting figures referenced in the text. This material is available free of charge via the Internet at http://pubs.acs.org.

JA905488X